Atom column detection from simultaneously acquired ABF and ADF STEM images

Atom column detection from simultaneously acquired ABF and ADF STEM images

J. Fatermans[a,b,c], A.J. den Dekker[c], K. Müller-Caspary[d], N. Gauquelin[a,b], J. Verbeeck[a,b], S. Van Aert[a,b,*]

[a]*Electron Microsopy for Materials Science (EMAT), University of Antwerp, Groenenborgerlaan 171, 2020 Antwerp, Belgium*
[b]*NANOlab Center of Excellence, University of Antwerp, Belgium*
[c]*imec-Vision Lab, University of Antwerp, Universiteitsplein 1, 2610 Wilrijk, Belgium*
[d]*Ernst Ruska-Centre for Microscopy and Spectroscopy with Electrons, Forschungszentrum Jülich, 52425 Jülich, Germany*

Abstract

In electron microscopy, the maximum a posteriori (MAP) probability rule has been introduced as a tool to determine the most probable atomic structure from high-resolution annular dark-field (ADF) scanning transmission electron microscopy (STEM) images exhibiting low contrast-to-noise ratio (CNR). Besides ADF imaging, STEM can also be applied in the annular bright-field (ABF) regime. The ABF STEM mode allows to directly visualize light-element atomic columns in the presence of heavy columns. Typically, light-element nanomaterials are sensitive to the electron beam, limiting the incoming electron dose in order to avoid beam damage and leading to images exhibiting low CNR. Therefore, it is of interest to apply the MAP probability rule not only to ADF STEM images, but to ABF STEM images as well. In this work, the methodology of the MAP rule, which combines statistical parameter estimation theory and model-order selection, is extended to be applied to simultaneously acquired ABF and ADF STEM images. For this, an extension of the commonly used parametric models in STEM is proposed. Hereby, the effect of specimen tilt has been taken into account, since small tilts from the crystal zone axis affect, especially, ABF STEM intensities. Using simulations as well as experimental data, it is shown that the proposed methodology can be successfully used to detect light elements in the presence of heavy elements.

Keywords: Scanning transmission electron microscopy (STEM), Annular bright-field (ABF), Annular dark-field (ADF), Statistical parameter estimation, Maximum a posteriori (MAP) probability

1. Introduction

Due to improvements in aberration correction technology, scanning transmission electron microscopy (STEM) has become a widely used technique to visualize nanomaterials down to sub-angstrom resolution [1, 2]. In particular, annular dark-field (ADF) imaging is a well-established imaging mode in STEM, in which the collection range of the annular detector lies outside of the illumination cone of the focused electron beam [3, 4]. The ADF STEM mode allows to obtain images with atomic resolution and exhibits a strong dependence on atomic number [5, 6]. Yet, merely visually interpreting high-resolution ADF images is insufficient to obtain precise structure information, which is crucial to fully understand the structure-properties relation of nanomaterials, since their physical and chemical properties are strongly dependent on their exact structural and chemical composition. Hence, a quantitative approach is required, which is provided by statistical parameter estimation theory [7–12]. Recently, it has been shown that the concepts of statistical parameter estimation in STEM can be combined with model-order selection, leading to the so-called maximum a posteriori (MAP) probability rule [13, 14]. This method allows to determine the structure of unknown nanomaterials in an automatic and objective manner and to detect atomic columns and even single atoms from high-resolution ADF STEM images with high reliability. The method is especially useful for the analysis of the structure of beam-sensitive materials. Due to the limited incoming electron dose that should be used to avoid beam damage, images of such materials typically exhibit low signal-to-noise ratio (SNR) and low contrast, and hence low contrast-to-noise ratio (CNR). As a result, a visual determination of the number of atomic columns in such images is unreliable and may lead to biased structure information.

In particular, the visualization of light-element atomic columns from ADF STEM images is challenging since light elements only scatter electrons weakly to high detector angles leading to low intensities in ADF images. As a result, light elements are barely visible and especially difficult to detect in the presence of heavy elements [13, 15, 16]. Interestingly, direct visualization of light elements has been enabled by the annular bright-field (ABF) mode in STEM where an annular detector spanning a range within the illumination cone of the electron beam is used [17, 18]. Due to the fact that ABF image contrast is less dependent on atomic number than ADF contrast [19, 20], light elements can be visualized better in the presence of heavy elements. This reduced dependence on atomic number, though, makes differentiating between atomic columns with close atomic numbers more difficult. In addition, due to

*Corresponding author
Email address: Sandra.VanAert@uantwerpen.be (S. Van Aert)

dynamical scattering, there is a non-monotonic intensity relationship with atomic number at all thicknesses. As a result, identifying the atom types of columns in an ABF image is not straightforward. Therefore, a simultaneous acquisition of both ABF and ADF STEM images is an interesting option to visualize atoms of a large range of atomic numbers for studying and interpreting materials at the atomic scale consisting of both light and heavy atoms. In case of beam-sensitive materials, the MAP probability rule [13, 14] can be used to determine the number of atomic columns for which there is most evidence in the simultaneously acquired ABF and ADF STEM image data.

Typically, the projected atomic columns in atomic resolution STEM images are modelled as Gaussian peaks superimposed on a constant background [12, 21, 22]. This methodology has been applied predominantly in the analysis of ADF STEM images [23–33], but it has also been used for obtaining quantitative information from ABF STEM images [34]. In the present paper, alternative parametric models for quantifying simultaneously acquired ABF and ADF STEM images are proposed by extending the commonly used parametric models in STEM. This results in alternative analytical expressions for the recently proposed MAP probability rule. Furthermore, it is shown that the proposed methodology allows to extend the concept of atom detectability [14] to simultaneously acquired ABF and ADF STEM image data. In addition to this, it is shown that the recently introduced ADF image-quality measure, namely the integrated CNR (ICNR) [14], also applies to ABF images and can be extended to simultaneously acquired ABF and ADF images.

This article is organized as follows. In section 2, the methodology to quantitatively analyze ABF and ADF STEM images simultaneously by the MAP probability rule is described in detail. This is followed in section 3 by showing that the concepts of atom detectability and ICNR, which were introduced for ADF STEM data, can be extended to simultaneously acquired ABF and ADF images as well. In section 4, the proposed method is applied to experimental images. Finally, in section 5, conclusions are drawn.

2. Methodology

2.1. Model-based parameter estimation

From the viewpoint of statistical parameter estimation theory, STEM images are considered as data planes from which unknown structure parameters need to be estimated. The starting point of this procedure is the construction of a parametric model that describes the expectations of the image pixel values as a function of unknown parameters. Then, quantitative structure information is obtained by fitting the model to the observed experimental data with respect to the unknown parameters using a criterion of goodness of fit. For atomic resolution STEM images, the projected atomic columns can be described as Gaussian peaks [12] since STEM intensities are sharply peaked at the atomic column positions [21, 22]. When the observed STEM pixel values of an image of $K \times L$ pixels are given by the vector $\boldsymbol{w} = (w_{11}, \ldots, w_{KL})^T$ and when each Gaussian peak is assumed to have a different width, the expectation model $f_{kl}(\boldsymbol{\theta})$, with $\boldsymbol{\theta}$ the vector of unknown parameters, describes the expectation of the observed pixel value w_{kl} at position (x_k, y_l):

$$f_{kl}(\boldsymbol{\theta}) = \zeta + \sum_{n=1}^{N} \eta_n exp\Big(- \frac{(x_k - \beta_{x_n})^2 + (y_l - \beta_{y_n})^2}{2\rho_n^2}\Big), \quad (1)$$

where ζ is a constant background, ρ_n, η_n, β_{x_n} and β_{y_n} are the width, the height and x- and y-coordinates of the nth atomic column described by a Gaussian peak, respectively, and N is the total number of atomic columns. The unknown parameters of the expectation model are represented by the parameter vector:

$$\boldsymbol{\theta} = (\beta_{x_1}, \ldots, \beta_{x_N}, \beta_{y_1}, \ldots, \beta_{y_N}, \rho_1, \ldots, \rho_N, \eta_1, \ldots, \eta_N, \zeta)^T. \quad (2)$$

For analyzing materials containing both light and heavy atoms, an interesting option is to acquire ABF and ADF STEM images simultaneously. As such, due to the simultaneous acquisition, a pixel at location (x_k, y_l) possesses both an ABF and ADF intensity. In order to obtain quantitative measurements from the ABF and ADF image data, statistical parameter estimation theory may be applied using a parametric model such as, for example, the one given by Eq. (1), as well as other similar models [12]. Although this methodology has up to now predominantly been applied to quantify ADF STEM images, it can be used to describe both ABF and ADF image data. For ADF STEM images, the atomic columns are modelled as Gaussian peaks with a positive height η since atomic columns in ADF STEM are depicted as bright spots on a dark background. Atomic columns in ABF STEM, though, are depicted as dark spots on a bright background. As a result, they are fitted by Gaussian peaks with a negative height η.

Nevertheless, a model such as the one given by Eq. (1) only allows to quantify an ABF or ADF STEM image independently of each other. To overcome this problem, the currently used models for quantifying STEM images need to be extended to fit both the ABF and ADF images simultaneously. This can be done by assuming that the Gaussian peaks describing a particular atomic column, one with negative height for the ABF image and one with positive height for the ADF image, are located at the same position, corresponding to the actual position of the projected atomic column. When the observed STEM pixel values of the ABF and ADF images are denoted as $\boldsymbol{w}^{ABF}$ and $\boldsymbol{w}^{ADF}$, respectively, and under the assumption that each estimated Gaussian peak has a different width, the extended expectation model $\boldsymbol{f}_{kl}(\boldsymbol{\theta})$, describing simultaneously acquired ABF and ADF STEM images, gives the expectation of the observed pixel values $\boldsymbol{w}_{kl} = (w_{kl}^{ABF}, w_{kl}^{ADF})$ at position (x_k, y_l):

$$\begin{aligned}\boldsymbol{f}_{kl}(\boldsymbol{\theta}) &= (f_{kl}^{ABF}, f_{kl}^{ADF}) \\ &= \Bigg(\zeta^{ABF} + \sum_{n=1}^{N} \eta_n^{ABF} exp\Big(- \frac{(x_k - \beta_{x_n})^2 + (y_l - \beta_{y_n})^2}{2(\rho_n^{ABF})^2}\Big), \\ &\quad \zeta^{ADF} + \sum_{n=1}^{N} \eta_n^{ADF} exp\Big(- \frac{(x_k - \beta_{x_n})^2 + (y_l - \beta_{y_n})^2}{2(\rho_n^{ADF})^2}\Big)\Bigg),\end{aligned} \quad (3)$$

where f_{kl}^{ABF} and f_{kl}^{ADF} denote the expectation models describing the ABF and ADF image, respectively. The parameters ζ^{ABF}

and ζ^{ADF} describe the constant background and ρ_n^{ABF}, ρ_n^{ADF}, η_n^{ABF}, η_n^{ADF} denote the widths and heights of the nth atomic column described by two Gaussian peaks, respectively, in both the ABF and ADF images. For the model given by Eq. (3), the unknown parameters are represented by the parameter vector:

$$\boldsymbol{\theta} = (\beta_{x_1},\ldots,\beta_{x_N},\beta_{y_1},\ldots,\beta_{y_N},\rho_1^{ABF},\ldots,\rho_N^{ABF},\rho_1^{ADF},\ldots,\rho_N^{ADF}, \eta_1^{ABF},\ldots,\eta_N^{ABF},\eta_1^{ADF},\ldots,\eta_N^{ADF},\zeta^{ABF},\zeta^{ADF})^T. \tag{4}$$

However, it is well known that the observed atomic column positions in ABF STEM images are sensitive to specimen tilt [35–37]. This causes a deviation of the observed positions from the actual positions of the projected atomic columns. The observed locations of the atomic columns in ADF STEM images, though, are less sensitive to specimen tilt and can be considered to be reliable indicators of the true column positions even in the presence of some tilt [19, 38, 39]. Thus, due to the effect of specimen tilt, the observed column positions in ABF STEM can be shifted as compared to the observed positions in ADF STEM. Since small tilts of the electron beam with respect to the crystal zone axis can easily be present in STEM experiments, it is important that the model that is fitted to the images accounts for the effect of the shifted observed column positions in ABF images. This will result in more accurate quantitative measurements. For this purpose, the expectation model proposed in Eq. (3) is modified by allowing the ABF peak locations to deviate from the ADF peak locations along the tilting direction:

$$\begin{aligned}\boldsymbol{f}_{kl}(\boldsymbol{\theta}) &= (f_{kl}^{ABF}, f_{kl}^{ADF}) \\ &= \Bigg(\zeta^{ABF} + \sum_{n=1}^{N} \eta_n^{ABF} exp\Big(-\frac{(x_k-\gamma_{x_n})^2+(y_l-\gamma_{y_n})^2}{2(\rho_n^{ABF})^2}\Big), \\ &\quad \zeta^{ADF} + \sum_{n=1}^{N} \eta_n^{ADF} exp\Big(-\frac{(x_k-\beta_{x_n})^2+(y_l-\beta_{y_n})^2}{2(\rho_n^{ADF})^2}\Big)\Bigg),\end{aligned} \tag{5}$$

with

$$(\gamma_{x_n},\gamma_{y_n}) = (\beta_{x_n}+\alpha_n cos\phi, \beta_{y_n}+\alpha_n sin\phi) \tag{6}$$

where ϕ and α_n indicate, respectively, the direction and amplitude of the shift of the nth Gaussian peak in the ABF image with respect to the corresponding peak in the ADF image. The amplitude of the shift is not necessarily equal or has the same sign for all atomic columns in the image, but depends on atom type and orientation [35–37]. This is due to the coherent image formation process in ABF STEM. In Eqs. (5) and (6), a conservative approach has been followed where no prior knowledge about the atom types and orientations is considered. This is the most general case where each atomic column possesses an individual amplitude of shift. Note that in Eq. (6) the shift of the ABF peaks only occurs along the tilting direction, as it is assumed that no atom position shift is observed in a direction perpendicular to this direction [35]. For the model given by Eq. (5) the parameter vector containing the unknown parameters is given by

Parameter	Symbol	Value
Acceleration voltage	V_0 (kV)	300
Defocus	ϵ (Å)	0
Spherical aberration	C_s (mm)	0.001
Spherical aberration of 5th order	C_5 (mm)	0
Semiconvergence angle	α (mrad)	22.9
ABF detector inner radius	β_1^{ABF} (mrad)	12
ABF detector outer radius	β_2^{ABF} (mrad)	22
ADF detector inner radius	β_1^{ADF} (mrad)	88
ADF detector outer radius	β_2^{ADF} (mrad)	98
Pixel size	$\Delta x = \Delta y$ (Å)	0.23
Number of scanned pixels	K×L	27×27
FWHM of the source image	FWHM (Å)	0.7

Table 1: Microscope parameter values for simulation of an ABF and ADF STEM image of a 10 nm thick $SrTiO_3$ unit cell using MULTEM including 5 mrad specimen tilt.

$$\boldsymbol{\theta} = (\beta_{x_1},\ldots,\beta_{x_N},\beta_{y_1},\ldots,\beta_{y_N},\rho_1^{ABF},\ldots,\rho_N^{ABF},\rho_1^{ADF},\ldots,\rho_N^{ADF}, \eta_1^{ABF},\ldots,\eta_N^{ABF},\eta_1^{ADF},\ldots,\eta_N^{ADF},\alpha_1,\ldots,\alpha_N,\phi,\zeta^{ABF},\zeta^{ADF})^T. \tag{7}$$

In order to verify whether the proposed parametric model in Eq. (5) is a valid model to describe images in the presence of tilt, a simulation of $SrTiO_3$ with a thickness of 10 nm has been performed using MULTEM [40, 41] with a specimen tilt of 5 mrad along the [010]-direction. The parameters of this simulation are included in Table 1. In Fig. 1, the arrangement of the Sr, Ti-O, and O columns is shown along with the simulated ADF and ABF STEM images in Figs. 1(a) and (b), respectively. First, these images have been analyzed using the parametric model including the effect of specimen tilt given by Eq. (5), where equal widths for the Gaussian peaks in the ABF image, ρ^{ABF}, and ADF image, ρ^{ADF}, have been used. The estimated column positions that follow from this approach are shown in Figs. 1(a) and (b) by red dots. It can be seen that there is a close correspondence between the estimated column positions and the true column positions, shown by green crosses, which have been determined by the atom positions of the top plane of the tilted specimen, considering the limited depth of focus in aberration-corrected STEM imaging [35]. In case the analysis is, instead, performed using a parametric model neglecting the effect of specimen tilt, such as the one given by Eq. (3), the estimated column positions deviate further from the true positions. This is shown in Figs. 1(a) and (b) where the estimated column positions using a model without taking specimen tilt into account are shown by yellow dots. Quantitatively, the average distance, including standard error, of the 9 estimated atomic column positions in the simulated image from their true column positions including the effect of specimen tilt is 8 ± 3 pm, whereas for neglecting tilt this is 18 ± 3 pm. This indicates that the atomic column locations, obtained from analyzing simultaneously acquired ABF and ADF STEM image data by the parametric model proposed in Eq. (5) including the effect of specimen tilt, correspond better to the true atomic column locations than the atom column positions obtained from analyzing the image data by a model neglecting the effect of specimen tilt. Furthermore, it is noted that by simultaneously analyzing

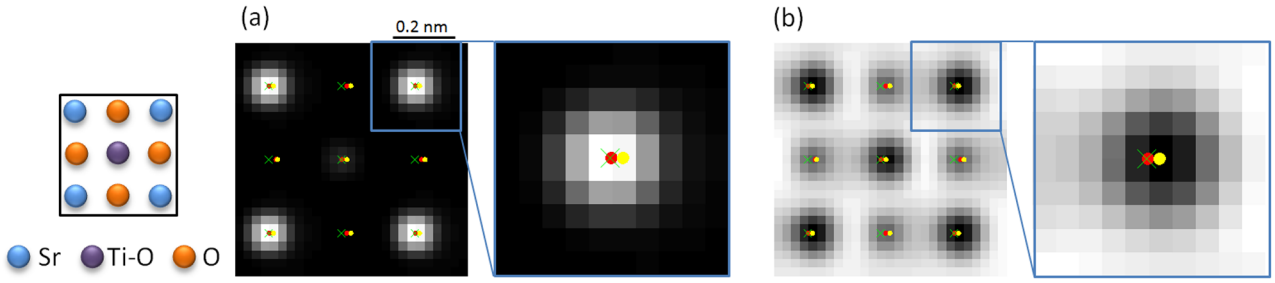

Figure 1: (a) Simulated ADF and (b) ABF STEM image of 10 nm-thick $SrTiO_3$ with a tilt angle of 5 mrad where the highlighted areas have been enlarged in the insets. The green crosses depict the true atomic column positions. The estimated atomic column positions obtained by performing model fitting including specimen tilt are shown by red dots, whereas for neglecting specimen tilt the estimated column positions are depicted by yellow dots. The inset on the left indicates the arrangement of the Sr, Ti-O, and O columns in (a) and (b).

ADF and ABF STEM image data more reliable atomic column position estimates can be obtained as compared to analyzing the images in a separate manner. By only taking into account the ADF STEM image data shown in Fig. 1(a) and by using a model such as the one given in Eq. (1), the average distance of the estimated positions of the O columns from their true column locations is 40 pm with a standard error of 20 pm. This deviation can be reduced by considering ABF STEM because this imaging mode is more suitable than ADF STEM for visualizing light elements, such as O. By only relying on the ABF STEM image data of Fig. 1(b) instead, the average distance, including standard error, of the estimated positions of the O columns from their true locations is 24.8 ± 0.8 pm. Although a great improvement as compared to ADF STEM can be achieved, the estimated atomic column positions that follow from ABF STEM are prone to the effect of specimen tilt. By simultaneously analyzing the ADF and ABF STEM image data using the proposed model in Eq. (5), the average distance of the estimated O column positions from their true locations is reduced to 16 pm with a standard error of 2 pm. The reason for this result lies in the fact that this model allows to take into account the improved light element signal of ABF STEM along with the effect of specimen tilt, which is otherwise not possible.

2.2. *Maximum a posteriori (MAP) probability*

In order to extract reliable structure information from simultaneously acquired ABF and ADF STEM images using either a model neglecting specimen tilt, such as in Eq. (3), or a model including tilt, such as in Eq. (5), knowledge about the number of atomic columns N present in the images is required. For beam-stable materials this number can be determined visually due to the high incoming electron dose that can be used to image these materials. Beam-sensitive nanostructures, such as specimens containing light elements, though, do not withstand a high incoming electron dose and, consequently, the dose should be limited in order to avoid beam damage resulting into images exhibiting low CNR. Since a simultaneous acquisition of ABF and ADF STEM images is, in particular, interesting for characterizing materials containing light elements, which are typically beam-sensitive, a visual inspection of such images may lead to biased results. To overcome this problem, the number of atomic columns N can be reliably quantified by the recently proposed MAP probability rule, which is a combination of statistical parameter estimation and model-order selection [13, 14], and which can be derived from Bayes' theorem [42]:

$$p(N|\boldsymbol{w}) = \frac{p(\boldsymbol{w}|N)p(N)}{p(\boldsymbol{w})}, \tag{8}$$

where $p(N|\boldsymbol{w})$ denotes the posterior probability of the presence of N atomic columns given the observed image pixel values $\boldsymbol{w}$. For a simultaneous aquisition of ABF and ADF images, $\boldsymbol{w}$ can be considered as the ensemble of the observed image pixel values of both images, $\{\boldsymbol{w}^{ABF}, \boldsymbol{w}^{ADF}\}$. The MAP probability rule evaluates the posterior probability $p(N|\boldsymbol{w})$ as a function of number of atomic columns N. As such, the most probable number of columns $\hat{N}$ in the image data can be selected corresponding to the maximum of $p(N|\boldsymbol{w})$. The term $p(\boldsymbol{w}|N)$ at the right-hand side of Eq. (8) reflects the evidence that the image data $\boldsymbol{w}$ is generated by N atomic columns. The probability $p(N)$ expresses prior knowledge of the number of atomic columns present in the image data. Assuming that there is no a piori preference for any number of columns, $p(N)$ can be described as a uniform distribution. The term in the denominator of Eq. (8) is merely a normalization constant, which is independent of the number of columns N, and, therefore, cancels out when comparing posterior probabilities as a function of N.

In order to acquire an expression for the posterior probability of the presence of N atomic columns given the observed image pixel values $\boldsymbol{w}$, $p(N|\boldsymbol{w})$, Eq. (8) is written as [14]

$$p(N|\boldsymbol{w}) \propto \int p(\boldsymbol{w}|\boldsymbol{\theta}, N)p(\boldsymbol{\theta}|N)d^M\boldsymbol{\theta}, \tag{9}$$

where the first term in the integral, $p(\boldsymbol{w}|\boldsymbol{\theta}, N)$, is the likelihood function which describes the probability of the observed image pixel values $\boldsymbol{w}$ for particular values of the parameters $\boldsymbol{\theta}$ of a model with N atomic columns. In essence, the likelihood function is a measure of the goodness of fit of the model with the experimental measurements or image pixel values. Since the dominant noise source in STEM imaging is statistical Poisson noise related to the process of electrons impinging onto the detector [43] and since the time between subsequent single electron impacts has been shown to fit a Poisson random process

[44], each observed image pixel value w_{kl} at position (x_k, y_l) is Poisson distributed [45, 46]. For an increasing expectation value $f_{kl}(\boldsymbol{\theta})$ of w_{kl}, the Poisson distribution tends to be a normal distribution with mean $\mu_{kl} = f_{kl}(\boldsymbol{\theta})$ and standard deviation $\sigma_{kl} = \sqrt{f_{kl}(\boldsymbol{\theta})}$ [47]. As such, when assuming that $\sigma_{kl} \approx \sqrt{w_{kl}}$ [14] and that the pixel values are statistically independent, the likelihood function for a STEM image can be expressed as

$$p(\boldsymbol{w}|\boldsymbol{\theta}, N) = \frac{e^{-\chi^2(\boldsymbol{\theta})/2}}{\prod_{k=1}^{K}\prod_{l=1}^{L}\sqrt{2\pi w_{kl}}}, \tag{10}$$

where

$$\chi^2(\boldsymbol{\theta}) = \sum_{k=1}^{K}\sum_{l=1}^{L}\frac{[w_{kl} - f_{kl}(\boldsymbol{\theta})]^2}{w_{kl}} \tag{11}$$

is a weighted sum-of-squared residuals misfit between the data and the parametric model. Since the noise for STEM images acquired with different detector geometries can be considered to be uncorrelated [48–50], it follows from Eq. (10) that the likelihood function for simultaneously acquired ABF and ADF STEM image data can be expressed as:

$$p(\boldsymbol{w}|\boldsymbol{\theta}, N) = \frac{e^{-\chi^2(\boldsymbol{\theta})/2}}{\prod_{k=1}^{K}\prod_{l=1}^{L}2\pi\sqrt{w_{kl}^{ABF}w_{kl}^{ADF}}}, \tag{12}$$

where

$$\chi^2(\boldsymbol{\theta}) = \sum_{k=1}^{K}\sum_{l=1}^{L}\left[\frac{[w_{kl}^{ABF} - f_{kl}^{ABF}]^2}{w_{kl}^{ABF}} + \frac{[w_{kl}^{ADF} - f_{kl}^{ADF}]^2}{w_{kl}^{ADF}}\right]. \tag{13}$$

The other term in the integral in Eq. (9), $p(\boldsymbol{\theta}|N)$, is the prior density of the parameters $\boldsymbol{\theta}$ for a model with N columns. Different expressions for the prior density function can be constructed reflecting different types of prior knowledge. Here, $p(\boldsymbol{\theta}|N)$ is expressed as a product of uniform distributions over a predefined range for each parameter θ_m in the model:

$$p(\boldsymbol{\theta}|N) = \begin{cases}\prod_{m=1}^{M}\frac{1}{\theta_{m_{max}} - \theta_{m_{min}}} & \text{for } m = 1, ..., M\text{: } \theta_{m_{min}} \leqslant \theta_m \leqslant \theta_{m_{max}} \\ 0 & \text{otherwise}\end{cases} \tag{14}$$

where the subscripts *max* and *min* refer to a predefined maximum and minimum value for each parameter, respectively. It has been shown that approximate analytical expressions for $p(N|\boldsymbol{w})$ can be derived for several parametric models to determine the number of atomic columns for which there is most evidence in ADF STEM image data [14]. From Eqs. (9), (12) and (14), following the same methodology, $p(N|\boldsymbol{w})$ for simultaneously acquired ABF and ADF STEM images using the model given by Eq. (3), neglecting the effect of specimen tilt, results into

$$p(N|\boldsymbol{w}) \propto \frac{N!}{[(\beta_{x_{max}} - \beta_{x_{min}})(\beta_{y_{max}} - \beta_{y_{min}})(\rho_{max}^{ABF} - \rho_{min}^{ABF})]^N} \times \frac{e^{-\chi^2_{min}/2}(4\pi)^{3N}[det(\nabla\nabla\chi^2)]^{-1/2}}{[(\rho_{max}^{ADF} - \rho_{min}^{ADF})(\eta_{max}^{ABF} - \eta_{min}^{ABF})(\eta_{max}^{ADF} - \eta_{min}^{ADF})]^N}, \tag{15}$$

where $\chi^2_{min} = \chi^2(\hat{\boldsymbol{\theta}})$, with $\hat{\boldsymbol{\theta}}$ the parameter vector that minimizes $\chi^2(\boldsymbol{\theta})$ given by Eq. (13) and where the term $\det(\nabla\nabla\chi^2) = \det\left(\frac{\partial^2\chi^2(\boldsymbol{\theta})}{\partial\boldsymbol{\theta}\partial\boldsymbol{\theta}^T}\Big|_{\boldsymbol{\theta}=\hat{\boldsymbol{\theta}}}\right)$ represents the determinant of the Hessian matrix of $\chi^2(\boldsymbol{\theta})$ evaluated at $\hat{\boldsymbol{\theta}}$. For the model given by Eq. (5), including the effect of tilt by taking into account the direction ϕ and amplitude α_n of the shift of the nth Gaussian peak in the ABF image with respect to the corresponding peak in the ADF image, the posterior probability becomes

$$p(N|\boldsymbol{w}) \propto \frac{N!(\alpha_{max} - \alpha_{min})^{-N}}{[(\beta_{x_{max}} - \beta_{x_{min}})(\beta_{y_{max}} - \beta_{y_{min}})(\rho_{max}^{ABF} - \rho_{min}^{ABF})]^N} \times \frac{e^{-\chi^2_{min}/2}(4\pi)^{3.5N}[det(\nabla\nabla\chi^2)]^{-1/2}}{[(\rho_{max}^{ADF} - \rho_{min}^{ADF})(\eta_{max}^{ABF} - \eta_{min}^{ABF})(\eta_{max}^{ADF} - \eta_{min}^{ADF})]^N}. \tag{16}$$

By using Eqs. (15) or (16), depending on the underlying parametric model, the MAP probability rule allows to select the most probable number of atomic columns $\hat{N}$ present in simultaneously acquired ABF and ADF STEM images, and hence the most probable atomic structure, by evaluating $p(N|\boldsymbol{w})$ as a function of N. The procedure for evaluating the MAP probability rule for simultaneously acquired ABF and ADF STEM images is equivalent to the one for single ABF or ADF STEM data [14]. Starting from an initial configuration containing N_0 peaks, the parameters $\boldsymbol{\theta}$ of the initial model are optimized by minimizing the weighted sum-of-squared residuals misfit $\chi^2(\boldsymbol{\theta})$, given by Eq. (13), subject to the constraint that $\boldsymbol{\theta}$ should belong to the support of the prior density function described by Eq. (14). Then, an extra peak is added to the initial configuration, so a model is constructed containing $N_0 + 1$ peaks. The parameters of this model are optimized according to the same procedure as described above. Hereby, the starting values of the peaks are based on the estimated parameter values of the previous estimation, in this case of a model with N_0 peaks. For the extra added peak, though, many different starting positions are tested to avoid ending up in a local minimum of $\chi^2(\boldsymbol{\theta})$. This procedure continues until the parameters of a model with N_{max} peaks are optimized. It should be noted that the MAP probability rule is not limited to the models given by Eqs. (3) and (5). Similar expressions as Eqs. (15) and (16) can be derived for other types of models as well.

3. Atom detectability, accuracy and precision

Recently, an alternative ADF STEM image-quality measure, ICNR, has been introduced that directly correlates with atom detectability [14]. This means that for increasing ICNR values, the probability of detecting an atom from the image data increases, and vice versa. The ICNR of an individual atomic column in an ADF STEM image is defined as follows [14]

$$ICNR = \frac{2\pi\eta^{ADF}(\rho^{ADF})^2}{[2\pi\eta^{ADF}(\rho^{ADF})^2 + \pi(3\rho^{ADF})^2\zeta^{ADF}]^{1/2}}, \tag{17}$$

where η^{ADF}, ρ^{ADF}, and ζ^{ADF} denote the estimated height and width of the column, and the background in the ADF image,

respectively. A similar expression for ICNR can also be defined for ABF STEM images:

$$ICNR = \frac{2\pi|\eta^{ABF}|(\rho^{ABF})^2}{[2\pi|\eta^{ABF}|(\rho^{ABF})^2 + \pi(3\rho^{ABF})^2(\zeta^{ABF} + \eta^{ABF})]^{1/2}}, \tag{18}$$

where, similarly as for Eq. (17), η^{ABF}, ρ^{ABF}, and ζ^{ABF} denote the estimated height and width of the column, and the background in the ABF image, respectively. Note that η^{ABF} in Eq. (18) has a negative value, because columns in ABF images are displayed as dark spots on a bright background. Although, at first sight, Eqs. (17) and (18) calculate the ICNR in a different way, they, in fact, represent the same formula. This can be better understood by considering the maximum pixel values, w_{max}^{ADF} and w_{max}^{ABF}, and minimum pixel values, w_{min}^{ADF} and w_{min}^{ABF}, of an ADF and ABF image, respectively, in the area around the column. As such, the following expressions hold:

$$\begin{aligned} w_{max}^{ADF} - w_{min}^{ADF} &\approx \eta^{ADF} \\ w_{max}^{ABF} - w_{min}^{ABF} &\approx |\eta^{ABF}| \\ w_{min}^{ADF} &\approx \zeta^{ADF} \\ w_{min}^{ABF} &\approx \zeta^{ABF} + \eta^{ABF}. \end{aligned} \tag{19}$$

From Eq. (19), Eqs. (17) and (18) can be rewritten in one expression as

$$ICNR \approx \frac{2\pi(w_{max} - w_{min})\rho^2}{[2\pi(w_{max} - w_{min})\rho^2 + \pi(3\rho)^2 w_{min}]^{1/2}}, \tag{20}$$

where w_{max} represents either w_{max}^{ADF} or w_{max}^{ABF}, w_{min} either w_{min}^{ADF} or w_{min}^{ABF}, and ρ either ρ^{ADF} or ρ^{ABF}, depending on what type of image is being analyzed.

For investigating atom detectability from simultaneously acquired ABF and ADF STEM data, an ABF and ADF image of an individual Si atom, deposited on a 5 nm amorphous C support, have been simulated using MULTEM. The amorphous C support has been obtained by placing C atoms on random positions within the volume of the layer, reaching a density of 2.2 g $\times$ cm^{-3} [51]. During this procedure a new C atom is only included if its distance with the other atoms is above a chosen minimal distance of 0.14 nm, which is slightly lower than the C-C bond length in graphene. The parameters of this simulation are listed in Table 2. A varying incoming electron dose has been applied to the simulated images in order to obtain a set of images containing different ICNR values, where a higher electron dose results in a higher ICNR value and a lower dose in a lower ICNR value. It is noted that in this procedure the simulated ABF and ADF STEM data are not necessarily subject to the same incoming electron dose. In this way, a great variety of ICNR values for the ABF and ADF images can be obtained. The ICNR of the ADF STEM images has been calculated using Eq. (17), whereas Eq. (18) has been used for the ABF STEM images. Each image obtained in this manner has been generated 100 times containing random Poisson noise.

Parameter	Symbol	Value
Acceleration voltage	V_0 (kV)	120
Defocus	ϵ (Å)	0
Spherical aberration	C_s (mm)	0.001
Spherical aberration of 5th order	C_5 (mm)	0
Semiconvergence angle	α (mrad)	21.0
ABF detector inner radius	β_1^{ABF} (mrad)	10
ABF detector outer radius	β_2^{ABF} (mrad)	20
ADF detector inner radius	β_1^{ADF} (mrad)	25
ADF detector outer radius	β_2^{ADF} (mrad)	100
Pixel size	$\Delta x = \Delta y$ (Å)	0.25
Number of scanned pixels	K×L	50×50
FWHM of the source image	FWHM (Å)	0.7

Table 2: Microscope parameter values for simulation of an ABF and ADF STEM image of an individual Si atom on a 5 nm C support using MULTEM.

Fig. 2(a) shows the observed detection rate of the Si atom, i.e. the number of times the atom can be successfully detected from the noise-disturbed simulated images by simultaneously analyzing the ABF and ADF STEM image data. The detection rate is displayed as a function of the ICNR of the ADF and ABF images, depicted as ICNR$^{\mathrm{ADF}}$ and ICNR$^{\mathrm{ABF}}$, respectively, and is calculated by the MAP probability rule given by Eq. (15) evaluated for $N = 0$ and $N = 1$ atomic columns. Hereby, a parametric model is used assuming the images of the atom to be Gaussian shaped, where the backgrounds ζ^{ADF} and ζ^{ABF}, and widths ρ^{ADF} and ρ^{ABF}, heights η^{ADF} and η^{ABF} and x- and y-coordinates β_x and β_y of the atom need to be estimated. It is clear from Fig. 2(a) that the detection rate decreases with decreasing ICNR values. Moreover, the circular symmetry indicates that atom detectability is independent of the exact ICNR$^{\mathrm{ADF}}$ and ICNR$^{\mathrm{ABF}}$ values as long as the square root of their quadratic sum remains unchanged. As a result, the concept of ICNR, which has been introduced for ADF STEM and which correlates image quality with atom detectability [14], can be extended for determining the combined quality of atomic columns in ABF and ADF STEM images:

$$ICNR = \sqrt{(ICNR^{ADF})^2 + (ICNR^{ABF})^2}. \tag{21}$$

From Fig. 2(a), it can be seen that from ICNR values of around 5.0 the detection rate of approximately 100 % starts dropping. As such, ICNR = 5.0 can be considered as a threshold value for reliable detection. It is stressed that Fig. 2(a) provides information on the probability of detecting an atom from simultaneously acquired ABF and ADF STEM image data. In order to make this possible, the methodology as described in section 2 is necessary since one cannot simply combine the atom detectability from ADF STEM with the one from ABF STEM in order to obtain the atom detectability of a simultaneous acquisition of ABF and ADF images. As such, Fig. 2(a) forms a natural extension of recent work where atom detectability has been correlated with the image quality of solely ADF STEM images [14].

Besides investigating atom detectability for a simultaneous analysis of ABF and ADF STEM images, also the accuracy and precision with which the atom positions are estimated can be evaluated. For this, the set of images of the Si atom on a 5 nm amorphous C support is used and analyzed in the same way as described above. Hereby, a model containing one atomic column has been considered. Accuracy and precision are investigated by calculating the squared distance between the estimated position of the Si atom $(\hat{\beta}_x, \hat{\beta}_y)$ and the true atom position (β_x, β_y) for each pair of noise-disturbed simulated ABF

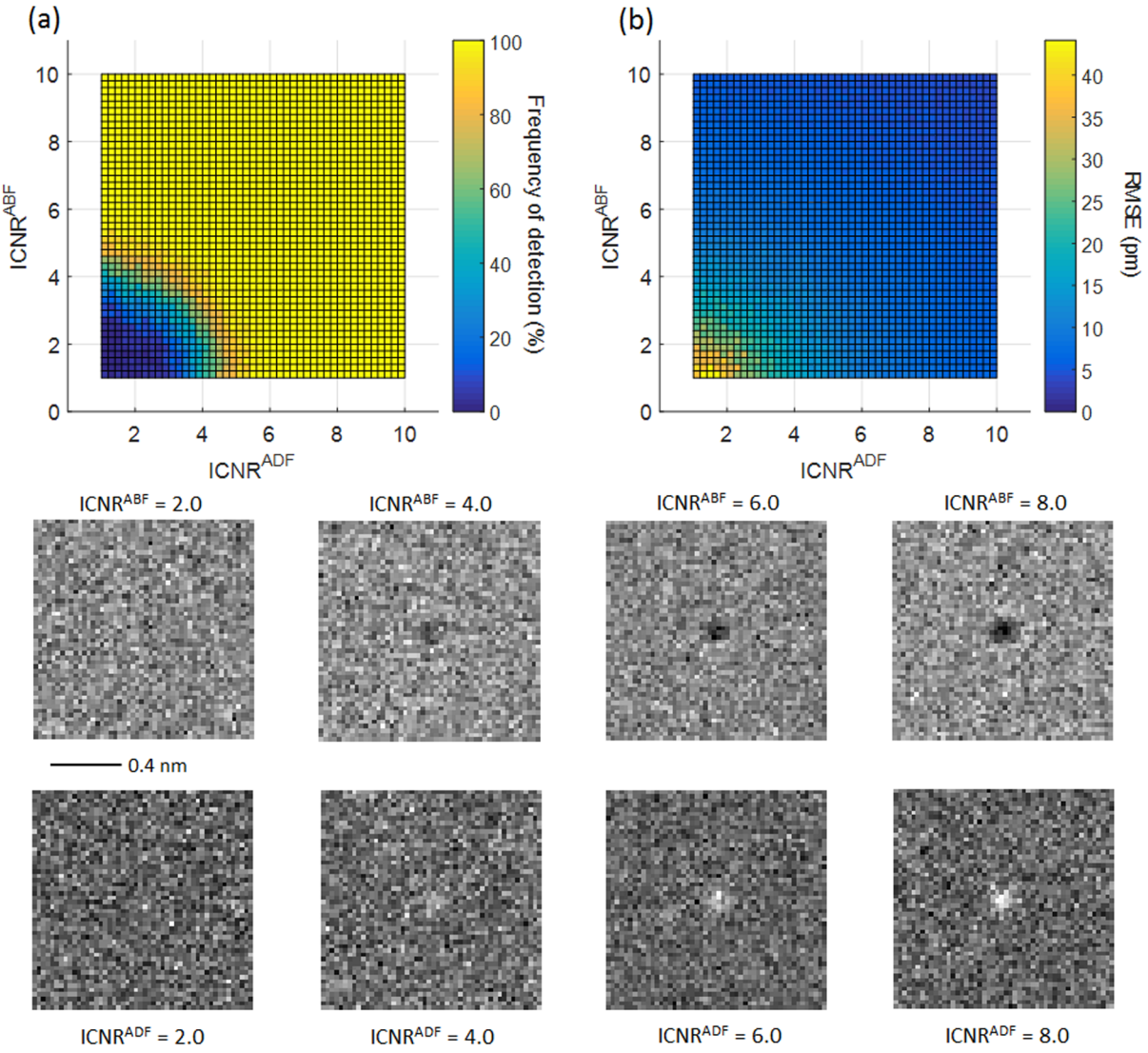

Figure 2: (a) Observed detection rate of a Si atom by the MAP probability rule and (b) RMSE of locating the Si atom from Poisson noise-disturbed simulated ABF and ADF STEM images as a function of $\mathrm{ICNR}^{\mathrm{ADF}}$ and $\mathrm{ICNR}^{\mathrm{ABF}}$ by simultaneous model fitting. The figures below show simulated ABF and ADF images, subject to Poisson noise, for different values of $\mathrm{ICNR}^{\mathrm{ABF}}$ and $\mathrm{ICNR}^{\mathrm{ADF}}$.

and ADF STEM images for all $\mathrm{ICNR}^{\mathrm{ADF}}$ and $\mathrm{ICNR}^{\mathrm{ABF}}$ combinations. When, for a certain $\mathrm{ICNR}^{\mathrm{ADF}}$ and $\mathrm{ICNR}^{\mathrm{ABF}}$ combination, the estimated atom position of the ith pair of noise-disturbed images is given by $(\hat{\beta}_{x_i}, \hat{\beta}_{y_i})$, the squared distance for this pair, d_i^2, is defined as

$$d_i^2 = (\hat{\beta}_{x_i} - \beta_x)^2 + (\hat{\beta}_{y_i} - \beta_y)^2. \tag{22}$$

By taking the square root of the average of d_i^2, one obtains an estimate of the root mean squared error (RMSE), which is a statistical measure of the deviation of the estimated atom position from the true position:

$$RMSE = \sqrt{\frac{1}{I}\sum_{i=1}^{I} d_i^2}, \tag{23}$$

with $I = 100$ for each combination of $\mathrm{ICNR}^{\mathrm{ADF}}$ and $\mathrm{ICNR}^{\mathrm{ABF}}$. Fig. 2(b) shows the estimated RMSE as a function of $\mathrm{ICNR}^{\mathrm{ADF}}$ and $\mathrm{ICNR}^{\mathrm{ABF}}$. It can be concluded that for increasing ICNR values the RMSE decreases, whereas for decreasing ICNR values the RMSE increases.

4. Experimental examples

In this section, the proposed methodology to detect atomic columns by the MAP probability rule from simultaneously acquired ABF and ADF STEM images is applied to two experimental examples exhibiting low CNR. Hereby, the effect of specimen tilt has been taken into account as small tilts might be present causing a possible shift of the measured atomic column locations in the ABF image as compared to the locations in the ADF image.

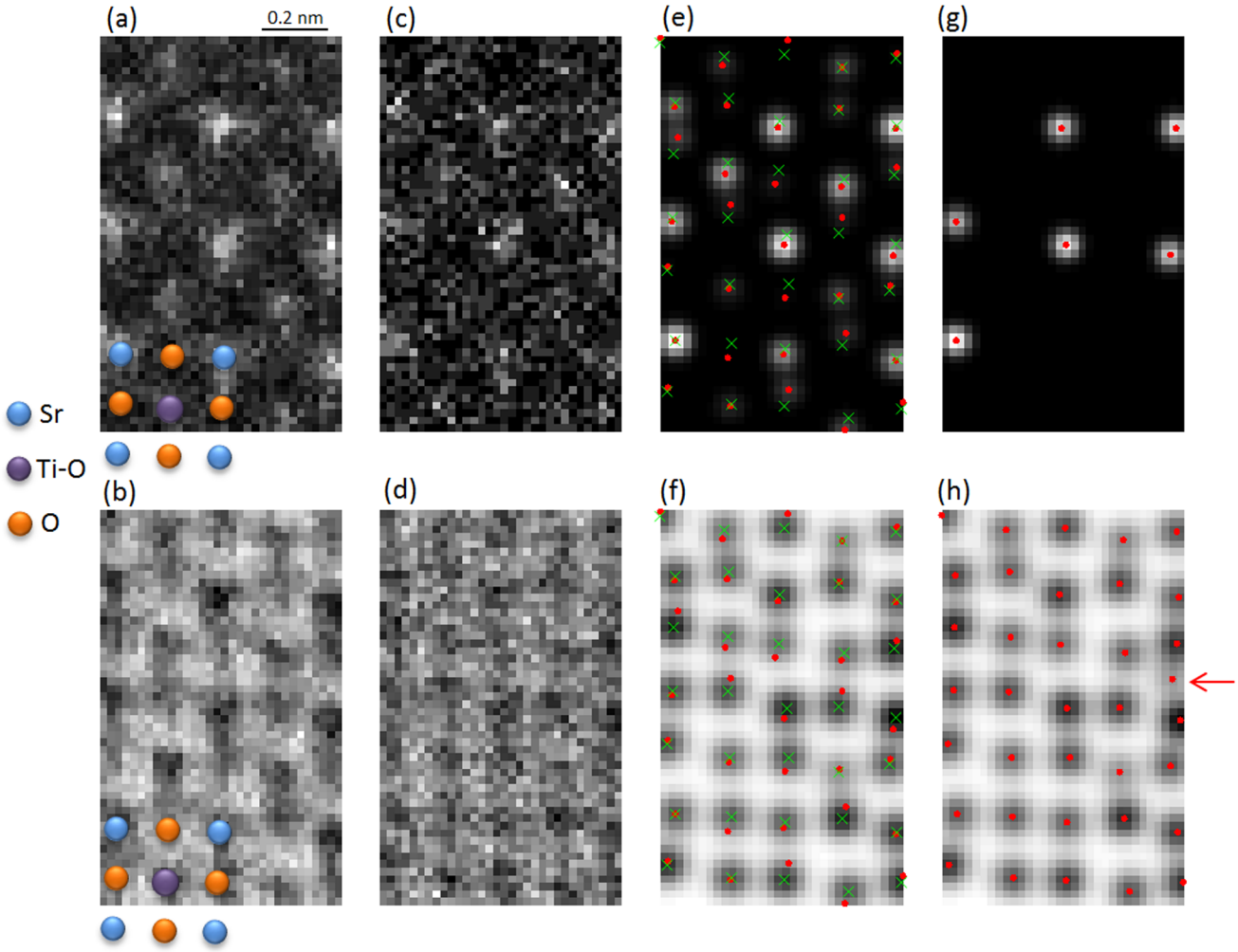

Figure 3: (a) Synthetic ADF and (b) ABF STEM image of $SrTiO_3$ obtained from an experimental 4D STEM dataset. (c) and (d) Noisier counterparts of (a) and (b), respectively. (e) and (f) Most probable refined models of the experimental ADF data in (c) and the ABF data in (d), respectively, obtained from the MAP probability rule by analyzing the data in (c) and (d) simultaneously taking into account specimen tilt. The red dots indicate the estimated column locations corresponding to the fitted ADF peak positions, whereas the green crosses correspond to the fitted ABF peak positions. (g) and (h) Most probable refined models by analyzing (c) and (d) independently of each other, where the red dots correspond to the fitted peak positions in the image data. The arrow in (h) indicates the detection of an extra column at a position where no column is expected.

4.1. $SrTiO_3$

Figs. 3(a) and (b) show reference synthetic ADF and ABF STEM images of $SrTiO_3$, respectively, where the Sr, Ti-O and O columns have been indicated, obtained from an experimental 4D STEM dataset [52] using a Medipix3 Quantum Detectors Merlin camera attached to a probe-corrected FEI Titan operated at 300 kV with a semi-convergence angle of 22.9 mrad. The camera frame time was 1 ms on top of a gap time of 412 μs due to read-out time imposed by the Medipix3 chip for acquisition in single pixel mode. The detector collection range for the ADF image has been chosen to be equal to 88-98 mrad, whereas the collection range for the ABF image is 12-22 mrad. Figs. 3(c) and (d) show noisier counterparts of Figs. 3(a) and (b), respectively, obtained by summing the electrons integrated over 10 equidistant detector rings with widths of 0.1 mrad separated by 1 mrad. The MAP probability rule for simultaneously acquired ABF and ADF STEM data has been applied to the images in Figs. 3(c) and (d), starting from an initial configuration of $N_0 = 0$ peaks, in order to obtain the number of atomic columns $\hat{N}$ for which there is most evidence in the image data, and, as a result, the most probable atomic structure. For this, the parametric model including the effect of specimen tilt given by Eq. (5) has been used, since tilt might be present, where widths ρ^{ABF} and ρ^{ADF} of the Gaussian peaks in the ABF image and ADF image, respectively, have been fitted, since the width of an atomic column is mainly determined by the finite source size and to a lesser extent by the atom type [53]. Hereby, it has been assumed that the shift of the ABF peaks from the ADF peak locations cannot exceed 50 pm, which is already a high value for typical shifts due to specimen tilt [35, 37]. This condition has been implemented by the prior density $p(\boldsymbol{\theta}|N)$, defined by Eq. (14), where the amplitudes of the shift α_n of Eq. (6) range from -50 up to +50 pm. The parameters ζ^{ABF}, η_n^{ABF}, ζ^{ADF}, and η_n^{ADF} range from 0 up to the maximum pixel

intensity of the ABF and ADF images, respectively, whereas the parameters ρ^{ABF}, ρ^{ADF}, β_{x_n}, and β_{y_n} range according to the field of view of the images. Lastly, the parameter ϕ in Eq. (6) ranges from 0 up to 2π. Figs. 3(e) and (f) show the most probable parametric models indicated by the MAP probability rule by simultaneously analyzing the ADF and ABF STEM image data of Figs. 3(c) and (d), respectively, consisting of $\hat{N} = 35$ atomic columns corresponding to the expected number of columns of $SrTiO_3$ in [100] direction. It is noted that in this analysis no prior knowledge about the expected locations of the atomic columns in $SrTiO_3$ has been taken into account and that imprecisions of the estimated atomic column positions may arise due to the limited dose conditions. The reason why the MAP probability rule is able to retrieve the atomic columns present in the image data is related to the ICNR values of the columns. The average ICNR values of each column type have been calculated, using Eq. (21), to be around 8.7, 6.0, and 7.4 for the Sr, Ti-O, and O columns, respectively. Considering the threshold value of ICNR = 5.0 for reliable detection mentioned in section 3, it follows that for these ICNR values, the MAP probability rule can reliably detect atomic columns from the ABF and ADF STEM data. In Figs. 3(e) and (f), the red dots correspond to the fitted ADF peak positions. Measured atomic column locations in ADF STEM are considered to be reliable indicators of the true column positions thanks to the insensitivity to specimen tilt [19, 38, 39]. It is noted that because of the elevated frame time, the unit cells may be distorted due to specimen drift [52] and that due to the limited electron dose conditions, imprecisions of the estimated atomic column positions may arise. In Figs. 3(g) and (h), the most probable refined models of the image data in Figs. 3(c) and (d), respectively, are shown, obtained by the MAP probability rule by analyzing the ADF and ABF image data independently of each other. For this, a parametric model such as given by Eq. (1) has been used, where widths ρ^{ABF} and ρ^{ADF} of the estimated Gaussian peaks in the ABF image and ADF image, respectively, have been assumed. From Fig. 3(g), it can be seen that only from analyzing the ADF STEM image only some of the Sr columns can be detected. This is due to the fact that the average ICNR value of all the Sr columns in the ADF image, calculated from Eq. (17), is around 4.0, which typically restricts a 100 % detection rate [14]. The average ICNR values in the ADF image of the other types of columns in $SrTiO_3$ are even lower, around 1.9 for the Ti-O and 0.6 for the O columns, restricting detection of these columns even further. The average ICNR values of the atomic columns in the ABF image, though, calculated from Eq. (18), are higher, around 7.7, 5.7, and 7.4 for the Sr, Ti-O, and O columns, respectively, improving their detectability. It can be seen from Fig. 3(h) that the expected atomic columns in $SrTiO_3$ are found. In this process, though, one atomic column, which has been indicated by the red arrow in Fig. 3(h), has been detected at a position where no column is expected. It is noted that this column is not detected when also the ADF STEM image data is taken into account in a simultaneous analysis, as shown in Fig. 3(f). In addition, although from analyzing the ABF image data in Fig. 3(d) independently of the ADF image data in Fig. 3(c) the atomic columns can be detected quite reliably, the estimated atomic column positions are prone to specimen tilt, since the ABF peak locations are sensitive to this effect. This may lead to biased structure information because the ABF peak locations are shifted from the true column positions. As shown in subsection 2.1 from the data in Fig. 1, more reliable atomic column position estimates can be obtained by combining the ABF and ADF STEM image information.

4.2. $LiMn_2O_4$

As another example, simultaneous ADF and ABF STEM images of $LiMn_2O_4$ have been acquired which are shown in Figs. 4(a) and (b), respectively, together with the spinel structure of $LiMn_2O_4$. Here, two annular detectors are used. One collects the electrons scattered toward high scattering angles, whereas the other is placed within the illumination cone of the electron probe. The images have been obtained by a probe-corrected FEI Titan operated at 300 kV with a semiconvergence angle of 19.8 mrad. The detector collection ranges for the ABF and ADF images are 8-17 mrad and 44-190 mrad, respectively. The average ICNR values of the Li, Mn, and O columns have been estimated by Eq. (21) to be around 7.7, 15.0, and 7.8, respectively, which is above the estimated threshold value of 5.0 for reliable detection. Analyzing Li-containing materials is of relevance since they have great technological interest because of their importance in battery devices [54, 55]. Therefore, the direct visualization of the Li atoms has been an important research topic in STEM and has been achieved by imaging in the ABF mode [56–60]. Nevertheless, materials containing light elements, such as Li, are sensitive to the electron beam. For such materials, beam damage is limited by imaging the specimen with a low incoming electron dose leading to images exhibiting low CNR. This is also the case for the images shown in Figs. 4(a) and (b) where the determination of the number of atomic columns and their positions is not straightforward by merely visually interpreting the image data. In order to overcome this problem, the MAP probability rule for simultaneously acquired ABF and ADF STEM images is applied to Figs. 4(a) and (b) by using the parametric model given by Eq. (5) including the effect of specimen tilt, since some tilt might have been present during the acquisition of the images. Similarly as for the example of $SrTiO_3$ in Fig. 3, the analysis was started from an initial configuration containing $N_0 = 0$ peaks and widths ρ^{ABF} and ρ^{ADF} of the Gaussian peaks in the ABF and ADF image, respectively, have been used. The shift of the ABF peaks from the ADF peak locations has been chosen not to be larger than 50 pm. Also for the other parameters the same ranges as in section 4.1 have been defined. Figs. 4(c) and (d) show the most probable parametric models indicated by the MAP probability rule for the ADF and ABF STEM image data of Figs. 4(a) and (b), respectively, consisting of 46 atomic columns. As already mentioned in the analysis of Fig. 3, also in this analysis imprecisions in the estimated atom positions may arise due to the finite dose conditions of Figs. 4(a) and (b). When one aims to determine the composition of the material, a subsequent analysis is needed. For this, the volumes under each estimated Gaussian peak describing an atomic column can be used to calculate the scattering cross section, which

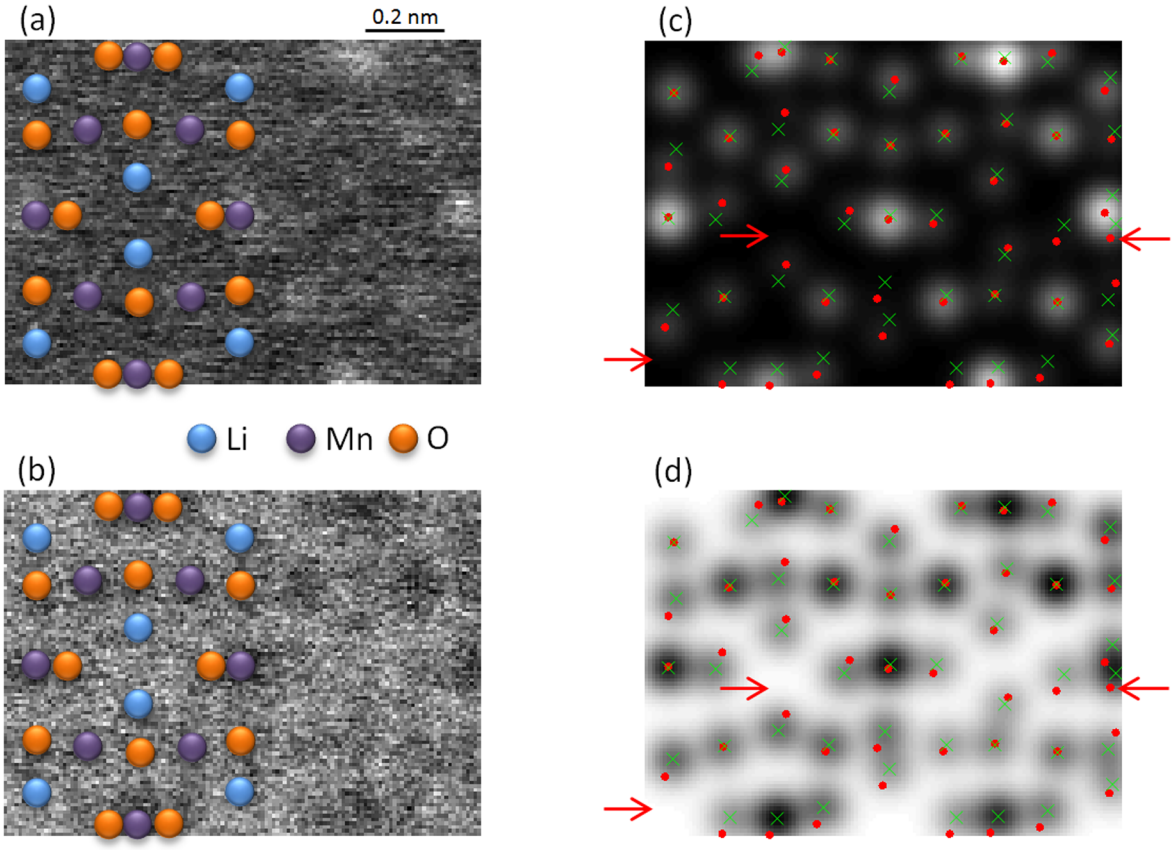

Figure 4: (a) Experimental ADF and (b) ABF STEM image of $LiMn_2O_4$ overlain with the spinel atomic arrangement. (c) Most probable refined model of the experimental ADF data in (a) and (d) most probable model of the ABF data in (b) obtained from the MAP probability rule by analyzing the data in (a) and (b) simultaneously taking into account specimen tilt. The red dots indicate the estimated column locations corresponding to the fitted ADF peak positions, whereas the green crosses correspond to the fitted ABF peak positions. The arrows in (c) and (d) indicate the expected locations of two columns that were not detected and the detection of an extra column at a position where no column is expected.

is defined as the total intensity of electrons scattered by a single atomic column [12, 23, 27, 61]. The detected number of $\hat{N} = 46$ atomic columns from Figs. 4(a) and (b) is slightly less than the expected 47 columns considering the spinel structure of $LiMn_2O_4$ since two columns were not detected and one extra column position was found in the experimental data. These columns have been indicated in Figs. 4(c) and (d) by red arrows. The reason why two atomic columns were not detected by the MAP probability rule, although expected by the spinel structure of $LiMn_2O_4$, is related to their ICNR values. It has been estimated by Eq. (21) that these columns exhibit ICNR values of around 5.4. From the analysis performed in section 3, shown in Fig. 2(a), it followed that for such ICNR values typically a detection rate of approximately 100 % cannot be attained. The observed reduced ICNR values at these sites may be caused by a reduced Li occupancy. The probability for over- or underfitting is an inherent limitation of model-order selection methods, like the MAP probability rule, and will generally increase with decreasing CNR. Despite this, the MAP probability rule has been able to retrieve a reliable representation of the atomic column locations in $LiMn_2O_4$ without including any prior information about the expected spinel atomic arrangement.

5. Conclusions

In the present paper, a new method for simultaneously analyzing ABF and ADF STEM images using statistical parameter estimation has been introduced. For this, the existing parametric models in STEM have been extended enabling the possibility to simultaneously analyze ABF and ADF image data. Hereby, the effect of specimen tilt, which shifts the ABF peak locations from the true atomic column locations, has been taken into account since small tilts of the electron beam with respect to the crystal zone axis can easily be present in STEM experiments. Furthermore, the recently proposed concept of atom detectability in ADF STEM and its relation with the image-quality measure ICNR [14] have been extended to the case of simultaneously analyzing both ABF and ADF STEM signals. In addition, it has been shown that the MAP probability rule [13, 14], which aims to determine the most probable atomic structure from images of beam-sensitive materials, can also be applied to the proposed framework of simultaneously fitting the ABF and ADF image data. This has been illustrated by using the MAP probability rule to investigate experimental STEM data, allowing to obtain a reliable estimation of atomic column locations. In this work, ABF and ADF STEM data has been

analyzed simultaneously, but, in principle, one is not limited to these angular detector ranges only. The proposed methodology can serve as a basis for extending model-based analysis to the entire STEM angular range and for applications in 4D STEM.

Acknowledgements

The authors acknowledge financial support from the Research Foundation Flanders (FWO, Belgium) through project fundings (No. W.O.010.16N, No. G.0368.15N, No. G.0502.18N, EOS 30489208). This project has received funding from the European Research Council (ERC) under the European Union's Horizon 2020 research and innovation programme (Grant Agreement No. 770887). The authors acknowledge funding from the European Union's Horizon 2020 research and innovation programme under grant agreement No. 823717 - ESTEEM3. The direct electron detector (Medipix3, Quantum Detectors) was funded by the Hercules fund from the Flemish Government. K. M. C. acknowledges funding from the Initiative and Network Fund of the Helmholtz Association (Germany) under contract VH-NG-1317. The authors thank Mark Huijben from the University of Twente (Enschede, The Netherlands) for providing the $LiMn_2O_4$ sample used in section 4.2 of this study. N. G., J. V., and S. V. A. acknowledge funding from the University of Antwerp through the Concerted Research Actions (GOA) project Solarpaint and the TOP project.

References

[1] H.H. Rose, Historical aspects of aberration correction, J. Elect. Microsc. 58 (2009) 77-85.

[2] P.W. Hawkes, The correction of electron lens aberrations, Ultramicroscopy 156 (2015) A1-A64.

[3] A.V. Crewe, J. Wall, J. Langmore, Visibility of single atoms, Science 168 (1970) 1338-1340.

[4] S.J. Pennycook, L.A. Boatner, Chemically sensitive structure-imaging with a scanning transmission electron microscope, Nature 336 (1988) 565-567.

[5] D.E. Jesson, S.J. Pennycook, Incoherent imaging of crystals using thermally scattered electrons, Proc. Roy. Soc. A 449 (1995) 273-293.

[6] P.D. Nellist, S.J. Pennycook, The principles and interpretation of annular dark-field Z-contrast imaging, Advances in Imaging and Electron Physics 113 (2000) 147-203.

[7] A.J. den Dekker, S. Van Aert, A. van den Bos, D. Van Dyck, Maximum likelihood estimation of structure parameters from high resolution electron microscopy images. Part I: A theoretical framework, Ultramicroscopy 104 (2005) 83-106.

[8] S. Van Aert, A.J. den Dekker, A. van den Bos, D. Van Dyck, J.H. Chen, Maximum likelihood estimation of structure parameters from high resolution electron microscopy images. Part II: A practical example, Ultramicroscopy 104 (2005) 107-125.

[9] A. van den Bos, Parameter estimation for scientists and engineers, Wiley, Hoboken, New Jersey, 2007.

[10] S. Van Aert, W. Van den Broek, P. Goos, D. Van Dyck, Model-based electron microscopy: from images toward precise numbers for unknown structure parameters, Micron 43 (2012) 509-515.

[11] A.J den Dekker, J. Gonnissen, A. De Backer, J. Sijbers, S. Van Aert, Estimation of unknown structure parameters from high-resolution (S)TEM images: What are the limits?, Ultramicroscopy 134 (2013) 34-43.

[12] A. De Backer, K.H.W. van den Bos, W. Van den Broek, J. Sijbers, S. Van Aert, StatSTEM: An efficient approach for accurate and precise model-based quantification of atomic resolution electron microscopy images, Ultramicroscopy 171 (2016) 104-116.

[13] J. Fatermans, A.J. den Dekker, K. Müller-Caspary, I. Lobato, C.M. O'Leary, P.D. Nellist, S. Van Aert, Single atom detection from low contrast-to-noise ratio electron microscopy images, Phys. Rev. Lett 121 (2018) 056101.

[14] J. Fatermans, S. Van Aert, A.J. den Dekker, The maximum a posteriori probability rule for atom column detection from HAADF STEM images, Ultramicroscopy 201 (2019) 81-91.

[15] M. Varela, A.R. Lupini, K. van Benthem, A.Y. Borisevich, M.F. Chisholm, N. Shibata, E. Abe, S.J. Pennycook, Materials characterization in the aberration-corrected scanning transmission electron microscope, Annual Review of Materials Research 35 (2005) 539-569.

[16] K.A. Mkhoyan, P.E. Batson, J. Cha, W.J. Schaff, J. Silcox, Direct determination of local lattice polarity in crystals, Science 312 (2006) 1354.

[17] E. Okunishi, I. Ishikawa, H. Sawada, F. Hosokawa, M. Hori, Y. Kondo, Visualization of light elements at ultrahigh resolution by STEM annular bright field microscopy, Microsc. Microanal. 15 (Suppl 2) (2009) 164-165.

[18] S.D. Findlay, N. Shibata, H. Sawada, E. Okunishi, Y. Kondo, T. Yamamoto, Y. Ikuhara, Robust atomic resolution imaging of light elements using scanning transmission electron microscopy, Appl. Phys. Lett. 95 (2009) 191913-1-191913-3.

[19] S.D. Findlay, N. Shibata, H. Sawada, E. Okunishi, Y. Kondo, Y. Ikuhara, Dynamics of annular bright field imaging in scanning transmission electron microscopy, Ultramicroscopy 110 (2010) 903-923.

[20] R. Brydson, Aberration-corrected analytical transmission electron microscopy, RMS-Wiley, Chichester, West Sussex, U.K., 2011.

[21] D. Van Dyck, High-resolution electron microscopy, Adv. Imaging Electron Phys. 123 (2002) 105-171.

[22] P.D. Nellist, Scanning transmission electron microscopy, in: P.W. Hawkes, J.H.C. Spence (Eds.), Science of Microscopy vol 1, Springer, New York, 2007, pp. 65-132, Ch. 2.

[23] S. Van Aert, J. Verbeeck, R. Erni, S. Bals, M. Luysberg, D. Van Dyck, G. Van Tendeloo, Quantitative atomic resolution mapping using high-angle annular dark field scanning transmission electron microscopy, Ultramicroscopy 109 (2009) 1236-1244.

[24] S. Van Aert, K.J. Batenburg, M.D. Rossell, R. Erni, G. Van Tendeloo, Three-dimensional atomic imaging of crystalline nanoparticles, Nature 470 (2011) 374-377.

[25] S. Bals, M. Casavola, M.A. Van Huis, S. Van Aert, K.J. Batenburg, G. Van Tendeloo, D. Vanmaekelbergh, Three-dimensional atomic imaging of colloidal core-shell nanocrystals, NanoLetters 11 (2011) 3420-3424.

[26] S. Bals, S. Van Aert, C.P. Romero, K. Lauwaet, M.J. Van Bael, B. Schoeters, B. Partoens, E. Yücelen, P. Lievens, G. Van Tendeloo, Atomic scale dynamics of ultrasmall germanium clusters, Nat. Comm. 3 (2012) 897.

[27] S. Van Aert, A. De Backer, G.T. Martinez, B. Goris, S. Bals, G. Van Tendeloo, A. Rosenauer, Procedure to count atoms with trustworthy single-atom sensitivity, Phys. Rev. B 87 (2013) 064107.

[28] G.T. Martinez, A. Rosenauer, A. De Backer, J. Verbeeck, S. Van Aert, Quantitative composition determination at the atomic level using model-based high-angle annular dark field scanning transmission electron microscopy, Ultramicroscopy 137 (2014) 12-19.

[29] P. Kundu, S. Turner, S. Van Aert, N. Ravishankar, G. Van Tendeloo, Atomic structure of quantum gold nanowires: quantification of the lattice strain. *ACS Nano*, 8 (2014), 599-606.

[30] H. Akamine, K.H.W. van den Bos, N. Gauquelin, S. Farjami, S. Van Aert, D. Schryvers, M. Nishidi, Determination of the atomic width of an APB In ordered CoPt using quantified HAADF STEM, J. Alloys and Compd. 644 (2015) 570-574.

[31] K.H.W. van den Bos, A. De Backer, G.T. Martinez, N. Winckelmans, S.Bals, P.D. Nellist, S. Van Aert, Unscrambling mixed elements using high angle annular dark field scanning transmission electron microscopy, Phys. Rev. Lett. 116 (2016) 246101.

[32] J. Gonnissen, D. Batuk, G.F. Nataf, L. Jones, A.M. Abakumov, S. Van Aert, D. Schryvers, E.K.H. Salje, Direct observation of ferroelectric domain walls in $LiNbO_3$: Wall-meanders, kinks, and local electric charges, Adv. Func. Mat. 26 (2016) 7599-7604.

[33] A. De Backer, L. Jones, I. Lobato, T. Altantzis, B. Goris, P.D. Nellist, S. Bals, S. Van Aert, Three-dimensional atomic models from a single projection using Z-contrast imaging: verification by electron tomography and opportunities. Nanoscale 9 (2017) 8791-8798.

[34] N. Gauquelin, K.H.W. van den Bos, A. Béché, F.F. Krause, I. Lobato, S. Lazar, A. Rosenauer, S. Van Aert, J. Verbeeck, Determining oxygen relaxations at an interface: A comparitive study between transmission electron microscopy techniques. Ultramicroscopy 181 (2017) 178-190.
[35] D. Zhou, K. Müller-Caspary, W. Sigle, F.F. Krause, A. Rosenauer, P.A. van Aken, Sample tilt effects on atom column position determination in ABF-STEM imaging. Ultramicroscopy 160 (2016) 110-117.
[36] H.G. Brown, R. Ishikawa, G. Sánchez-Santolino, N.R. Lugg, Y. Ikuhara, L.J. Allen, N. Shibata, A new method to detect and correct sample tilt in scanning transmission electron microscopy bright-field imaging. Ultramicroscopy 173 (2017) 76-83.
[37] P. Gao, A. Kumamoto, R. Ishikawa, N. Lugg, N. Shibata, Y. Ikuhara, Picometer-scale atom position analysis in annular bright-field STEM imaging. Ultramicroscopy 184 (2018) 177-187.
[38] S.E. Maccagnano-Zacher, K.A. Mkhoyan, E.J. Kirkland, J. Silcox, Effects of tilt on high-resolution ADF STEM imaging. Ultramicroscopy 108 (2008) 718-726.
[39] Y.-G. So, K. Kimoto, Effect of specimen misalignment on local structure analysis using annular dark-field imaging. J. Electron Microsc. 61 (2012) 207-215.
[40] I. Lobato, D. Van Dyck, MULTEM: A new multislice program to perform accurate and fast electron diffraction and imaging simulations using Graphics Processing Units with CUDA, Ultramicroscopy 156 (2015) 9-17.
[41] I. Lobato, S. Van Aert, J. Verbeeck, Progress and new advances in simulating electron micrscopy datasets using MULTEM, Ultramicroscopy 168 (2016) 17-27.
[42] D.S. Sivia, J. Skilling, A Bayesian tutorial, Oxford University Press, New York, 2006.
[43] T. Seki, Y. Ikuhara, N. Shibata, Theoretical framework of statistical noise in scanning transmission electron microscopy, Ultramicroscopy 193 (2018) 118-125.
[44] X. Sang, J.M. LeBeau, Characterizing the response of a scintillator-based detector to single electrons, Ultramicroscopy 161 (2016) 3-9.
[45] A. Mood, F. Graybill, D. Boes, Introduction to the theory of statistics, 3rd edition, McGraw-Hill, Tokyo, Japan, 1974.
[46] A. van den Bos, A.J. den Dekker, Resolution considered - conventional approaches and an alternative, in: P.W. Hawkes (Ed.), Advances in imaging and electron physics, vol. 117, Academic Press, San Diego, 2001.
[47] A. Papoulis, S.U. Pillai, Probability, random variables, and stochastic processes, McGraw-Hill, New York, 2002.
[48] H. Rose, Phase contrast in scanning transmission electron microscopy, Optik 39 (1974) 416-436.
[49] M. Hammel, H. Rose, Optimum rotationally symmetric detector configurations for phase-contrast imaging in scanning transmission electron microscopy, Ultramicroscopy 58 (1995) 403-415.
[50] H.G. Brown, A.J. D'Alfonso, Z. Chen, A.J. Morgan, M. Weyland, C. Zheng, M.S. Fuhrer, S.D. Findlay, L.J. Allen, Structure retrieval with fast electrons using segmented detectors, Phys. Rev. B 93 (2016) 134116.
[51] C. Ricolleau, Y. Le Bouar, H. Amara, O. Landon-Cardinal, D. Alloyeau, Random vs realistic amorphous carbon models for high resolution microscopy and electron diffraction, J. Appl. Phys. 114 (2013) 213504.
[52] K. Müller-Caspary, F.F. Krause, F. Winkler, A. Béché, J. Verbeeck, S. Van Aert, A. Rosenauer, Comparison of first moment STEM with conventional differential phase contrast and the dependence on electron dose, Ultramicroscopy 203 (2019) 95-104.
[53] J. M. LeBeau, S. Stemmer, Experimental quantification of annular dark-field images in scanning transmission electron microscopy, Ultramicroscopy 108 (2008) 1653-1658.
[54] H. Li, Z. Wang, L. Chen, Research on advanced materials for Li-ion batteries, Advanced Materials 21 (2009) 4593-4607.
[55] N. Nitta, F. Wu, J.T. Lee, Li-ion battery materials: present and future, Materials Today 18 (2015) 252-264.
[56] Y. Oshima, H. Sawada, F. Hosokawa, E. Okunishi, T. Kaneyama, Y. Kondo, S. Niitaka, H. Takagi, Y. Tanishiro, K. Takayanagi, Direct imaging of lithium atoms in LiV_2O_4 by spherical aberration-corrected electron microscopy, Journal of Electron Microscopy 59 (2010) 457-461.
[57] R. Huang, T. Hitosugi, S.D. Findlay, C.A.J. Fisher, Y.H. Ikuhara, H. Moriwake, H. Oki, Y. Ikuhara, Real-time direct observation of Li in $LiCoO_2$ cathode material, Appl. Phys. Lett. 98 (2011) 051913.
[58] L. Gu, C. Zhu, H. Li, Y. Yu, C. Li, S. Tsukimoto, J. Maier, Y. Ikuhara, Direct observation of lithium staging in partially delithiated $LiFePO_4$ at atomic resolution, J. Am. Chem. Soc. 133 (2011) 4661-4663.
[59] X. He, L. Gu, C. Zhu, Y. Yu, C. Li, Y.-S. Hu, S. Tsukimoto, J. Maier, Y. Ikuhara, X. Duan, Direct imaging of lithium ions using aberration corrected annular-bright-field scanning transmission electron microscopy and associated contrast mechanisms, Mater. Express 1 (2011) 43-50.
[60] S. Lee, Y. Oshima, H. Sawada, F. Hosokawa, E. Okunishi, T. Kaneyama, Y. Kondo, S. Nikita, H. Takagi, Y. Tanishiro, K. Takayanagi, Counting lithium ions in the diffusion channel of a LiV_2O_4 crystal, Journal of Applied Physics 109 (2011) 113530.
[61] H. E., K.E. MacArthur, T.J. Pennycook, E. Okunishi, A.J. D'Alfonso, N.R. Lugg, L.J. Allen, P.D. Nellist, Probe integrated scattering cross sections in the analysis of atomic resolution HAADF STEM images, Ultramicroscopy 133 (2013) 109-119.